CHALMERS
UNIVERSITY OF TECHNOLOGY

Millimeter-Wave Quasi-Optical Feeds for Linear Array Antennas in Gap Waveguide Technology

Millimeter-Wave Quasi-Optical Feeds for Linear Array Antennas in Gap Waveguide Technology

Artem R. Vilenskiy*, Yingqi Zhang*, Esmé Galesloot†, Adrianus Bart Smolders†, Marianna V. Ivashina*
*Electrical Engineering Department, Chalmers University of Technology, 41296 Gothenburg, Sweden
artem.vilenskiy@chalmers.se
†Electromagnetics Group, Eindhoven University of Technology, 5612 Eindhoven, The Netherlands

***Abstract*—A realization of the quasi-optical (QO) feed concept for linear millimeter-wave (sub-)array antennas is demonstrated in gap waveguide technology. The proposed feed architecture employs an input transition from a ridge gap waveguide (RGW) to a groove gap waveguide (GGW), a radial (H-plane sectoral) GGW section, and a transition to an output RGW array. A design decomposition approach is presented to reduce simulation complexity. Several 20-element QO feed implementations are investigated at W-band demonstrating a 20% relative bandwidth (85–105 GHz), 0.5 dB insertion loss, and a capability of an amplitude taper control within the 10–20 dB range.**

***Index Terms*—quasi-optical feed, array antenna, gap waveguide, radial waveguide, metamaterials.**

I. Introduction

The fast development of modern mobile communication networks, radar and sensing systems determines the growing demand in millimeter(mm)-wave antenna solutions [1], [2]. High mm-wave frequency bands, such as W- and D-band, are of particular interest for existing and envisioned radio applications due to a wide available frequency bandwidth, relatively low atmospheric attenuation, high spatial resolution and positioning accuracy that could be achieved for physically small antenna terminals. On the other hand, a high free-space path loss and limited power-generation capabilities can significantly reduce system operation range at these frequencies. In view of these factors, high-gain phased array antennas (PAAs) with a versatile dynamic beam control have been largely exploited for such systems at high mm-wave frequencies [3]. A design complexity is another severe challenge that makes many traditional PAA architectures unavailable due to high production cost and/or tight manufacturing tolerances. Today, probably the most popular W/D-band PAA solutions employ the antenna-on-chip (AoC) and antenna-in-package (AiP) technologies [4]. However, despite high integration potential and affordability, AoC and AiP implementations are typically narrowband, limited in beam-steering range and radiation efficiency.

Recently, we have proposed a linear (sub-)array concept combining a low-order (1-bit) phase resolution and a spatial quasi-optical (QO) beamforming network [5]. This PAA concept is illustrated in Fig. 1a where an array of N_x radiating elements with integrated 1-bit phase shifters is excited through a QO tapered feed. As shown in [5] based on the approach

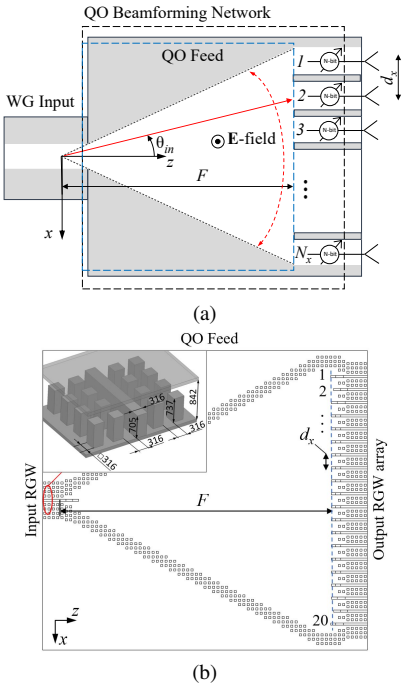

Fig. 1. (a) A linear (sub-)array antenna with a QO beamforming network comprising a QO feed and N-bit integrated phase shifters [5]. (b) An implementation of the QO feed in GWG technology. The inset demonstrates a basic RGW structure (units: μm).

developed in [6], the QO feed can be effectively used as a low-loss alternative to conventional corporate PAA feeds, with its non-linear output phase distribution being deliberately utilized for phase quantization errors randomization.

In this contribution, we concentrate on a gap waveguide (GWG) QO feed implementation at W-band (85 – 105 GHz), as demonstrated in Fig. 1b. The GWG technology [7], utilizing a 2-D electromagnetic bandgap (EBG) surface (bed of nails in this study) between two parallel metal plates to stop electromagnetic waves propagation, can offer low-loss contactless waveguiding and radiating structures. In [8], we demonstrated a GWG array element design that can be co-integrated with phase-shifting electronics and thus be employed in beam-steering PAAs as opposed to most reported GWG antennas that are fixed-beam. In this way, the GWG QO feed can be used to realize a complete beam-steering W-band PAA system with a fully contactless design greatly alleviating manufacturing and

assembling tolerances. Previously, several GWG H-plane horn antennas, employing tapering ridge gap waveguide (RGW), have been reported [9], [10]. In the case of a linear PAA, a wideband impedance matching between a tapering RGW and an array of the output channels is complicated. In that regard, in this study, we propose a QO feed based on a radial (sectoral) groove gap waveguide (GGW) connecting an array of output RGW channels with an RGW input. In particular, the following technical problems will be addressed: (i) impedance matching of the RGW input and output channels; (ii) compensation of an edge elements mismatch; (iii) minimization of transmission coefficients frequency ripples; (iv) controlling the QO feed output amplitude and phase distributions.

II. GWG Quasi-Optical Feed Design

The proposed design is based on the bed of nails EBG surface that forms sidewalls of both the RGW and radial GGW. Main design dimensions are presented in the inset of Fig. 1b. A single-mode operation bandwidth of the basic RGW spans 80–160 GHz. A dispersion diagram and losses analysis for this RGW can be found in [11]. Thus, the QO feed comprises three main parts: (i) the input basic RGW with a transition to the GGW input; (ii) the linearly tapering or radial GGW; (iii) the array of the output RGWs with transitions to the radial GGW output. An inter-element spacing of the output array $d_x = 1.896\,\text{mm} = 0.6\lambda_0$, where λ_0 is the free-space wavelength at the central design frequency $f_0 = 95$ GHz. The targeted design bandwidth is 85 – 105 GHz.

As discussed in [5], [6], for PAAs with a low-order phase resolution (e.g., 1-bit) a crucial design parameter is the QO feed focal ratio $F/(N_x d_x)$, where F is the focal distance (Fig. 1a). In the case of the 1-bit phase control, the optimum focal ratio is around 0.8 – 1.0 for a 10 – 20 dB amplitude taper. In this study, the focal ratio has been chosen as 1.0 (a GGW sidewalls tapering angle is 26.5°) that allows having a regular widening of the GGW, where for each two EBG periods ($P_{EBG} = 0.632$ mm) along z-axis the sidewall shifts for one period along x-axis. It helps to generate a more homogeneous field in the GGW area, which results in stabilized transmission coefficients over frequency.

Since a direct optimization of the QO feed with $N_x = 20$ represents an electrically large simulation problem, we have developed a decomposition approach allowing a separate design of the input and output GGW-to-RGW transition structures. That will be detailed in the following subsections. For all simulation models, aluminum has been used with 0.5-μm surface roughness (Groisse model).

A. Output RGW-to-GGW Transition: Central Elements

The receiving performance of the central output RGW channels can be simulated using the reciprocity principle by representing the channel as an element of an infinite transmitting 1-D array. Fig. 2 illustrates such simulation model with assigned sidewall ($\pm x$-direction) periodic boundary conditions (PBC), absorbing boundary conditions (ABC) in front ($-z$-direction) of the element, and aluminum walls at $\pm y$-direction.

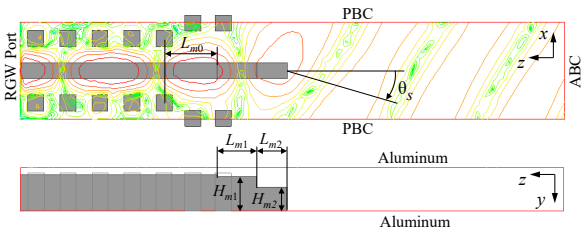

Fig. 2. The output RGW element in the infinite 1-D array environment. The overlapping E-field distribution (top plot) is given at 95 GHz and $\theta_s = 30°$.

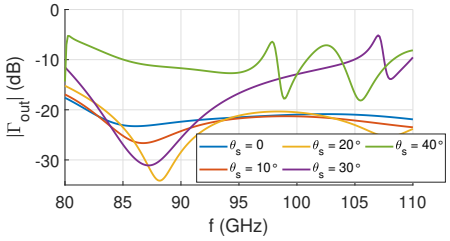

Fig. 3. Frequency dependencies of the output periodic element's active reflection coefficient for different scan angles θ_s. Design parameters (in μm): $L_{m0} = 1051$, $L_{m1} = 777$, $L_{m2} = 602$, $H_{m1} = 665$, $H_{m2} = 457$.

Thus, optimizing element's active reflection coefficient Γ_{out} for a given scan angle θ_s results in the matched receiving of an incident wave from the $\theta_{in} = \theta_s$ direction (inside the QO feed), as depicted in Fig. 1a. To provide a required impedance matching, we have introduced a wideband matching circuit comprising a 2-step RGW impedance transformer and an EBG sidewalls transition from the 2- to a 1-pin configuration. Fig. 3 shows the final Γ_{out} for different θ_s after a full-wave model optimization in Ansys HFSS. As seen, the element is well-matched for $\theta_s \leq 30°$. When θ_s approaches $40°$, the impedance matching significantly degrades, which resembles the scan blindness phenomenon in conventional 2-D arrays [12]. In such the 1-D array this effect can be expected when an equivalent grating-lobe-free condition $\sin(\theta_s) < \lambda/d_x - 1$ (λ is a free-space wavelength) is violated. The latter limits a minimum $F/(N_x d_x)$ for a given d_x/λ_0.

B. Output RGW-to-GGW Transition: Edge Elements

For the output RGW elements positioned close to the edge, the PBC imposed in Section II-A are not relevant due to the proximity of the GGW sidewalls. A 5-element full-wave model has been created to reconstruct the edge elements operation conditions. Fig. 4 depicts the model for three various configurations (O1 – O3) of the QO feed edge area. The first three edge elements have unique parameters of the matching circuit, whereas elements 4 and 5 are fully identical to the central element. In the xz-plane, the model is surrounded by the ABC.

The designs of the edge elements have been optimized by minimizing their $|\Gamma_{out}|$ for the case of scanning along the $\theta_s = 26.5°$ direction (parallel to the sidewall):

$$\Gamma_{out\,m} = \sum_{n=1}^{5} S^e_{mn} \exp\left(-j(n-m)k_x d_x\right),\ m = 1...3, \quad (1)$$

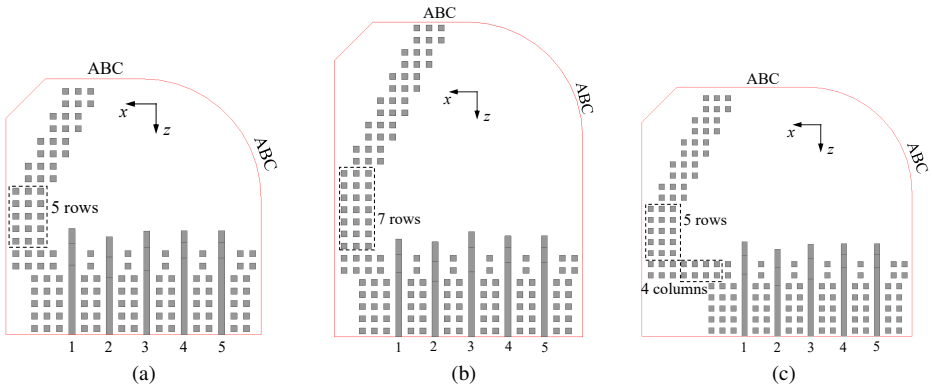

Fig. 4. Different configurations of the QO feed edge area: (a) configuration #1 (O1) – 5 additional rows of pins; (b) configuration #2 (O2) – 7 additional rows of pins; (c) configuration #3 (O3) – 5 additional rows and 4 columns of pins.

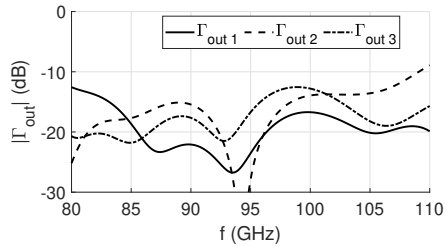

Fig. 5. Active reflection coefficients for the edge elements of the configuration O1 (Fig. 4a), $\theta_s = 26.5°$. Design parameters (in μm): $L_{m0}^{(1,2,3)} = 693, 68, 417$, $L_{m1}^{(1,2,3)} = 1077, 1026, 1159$, $L_{m2}^{(1,2,3)} = 765, 1028, 826$, $H_{m1}^{(1,2,3)} = 658, 632, 647$, $H_{m2}^{(1,2,3)} = 434, 477, 462$.

where $[S^e]$ is the S-matrix of the 5-port network; $k_x = 2\pi/\lambda \sin(\theta_s)$. Optimized Γ_{out} for the output configuration #1 is shown in Fig. 5. In general, a well-matched performance can be achieved for the elements of all configurations. However, each configuration, as will be shown in Section III, has a different effect on the overall QO feed characteristics.

C. Input RGW-to-GGW Transition

A separate model for the input transition has been developed to optimize input impedance matching and investigate the primary (illumination) field of the QO feed. Fig. 6 details three different input configurations (I1 – I3). The model is surrounded by the ABC in the xz-plane. The three designs exploit the same structure of the wideband impedance-matching circuit (Fig. 2). The crucial difference between the configurations is the organization of the RGW-to-GGW transition, which is created by an opening of the input RGW sidewalls. For I1, the transition is formed by $1.5P_{EBG}$ shift of the one row of pins, whereas the following three rows are shifted by P_{EBG} (one-and-three scheme). The two-and-two scheme ($1.5P_{EBG}$ first row shift) is used for the I2 that allows having a wider first GGW section. Finally, the widest input GGW ($2.5P_{EBG}$ first row shift) is utilized in I3 together with the two-and-two scheme.

A good impedance matching performance has been achieved for all configurations as shown in Fig. 7. From the electromagnetic perspective, the input RGW-to-GGW transition can be seen as: (i) a transition from the input RGW to a stepped rectangular GGW; (ii) a transition from the stepped GGW to the radial (H-plane sectoral) GGW when the local transverse size of the GWG is much larger than $2P_{EBG}$. Thereby, a transverse structure of the primary field will be defined by an excited modal content of the radial GGW, which, in turn, depends on a modal content excited in the stepped GGW. The latter will be demonstrated below.

III. Full QO Feed Performance

A. Frequency Performance

We have designed several QO feeds using different combinations of the input and output transition configurations. Three exemplary designs are demonstrated in Fig. 8 together with simulated magnitudes of S-parameters. In all cases, output configuration O1 has been used. As seen, the input configuration I1 realizes the minimum output amplitude taper. The modal content of the radial GGW predominantly consists of TE_{01} and TE_{03} modes (with respect to the radial direction) that effectively increases illumination of the edge elements. At the same time, the I2 configuration excites mainly TE_{01}, which results in a higher amplitude taper. When the wide I3 configuration is used, the input stepped rectangular GGW becomes over-moded, with both TE_{10} and TE_{30} (with respect to z-axis) excited. In the radial waveguide, this initial GGW field generates a complex multi-modal field content with high directivity determining a very high amplitude taper. Summarizing, it was found that the configurations I1O1 and I2O1 realize a good transmission flatness over frequency with the maximum ripple below ± 1 dB (85 – 105 GHz range).

To demonstrate the effect of the edge elements matching, we have simulated the I2O1 QO feed where all output RGW elements have the same (periodic model) matching circuit. Results, presented in Fig. 9a, clearly demonstrate the increase in frequency ripples for the edge elements transmission coefficients. It was also found that the the output configuration O3 noticeably deteriorates the transmission performance flatness (Fig. 9b) due to significant field reflections from the extended corner regions. In all considered cases, a simulated dissipative loss is below 0.5 dB.

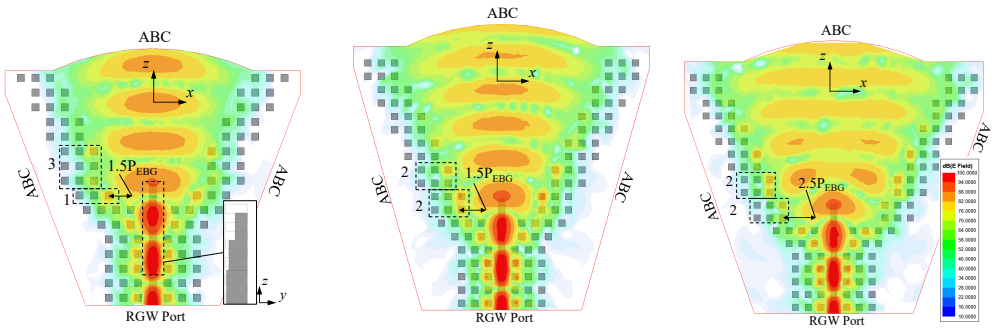

Fig. 6. Different configurations of the QO feed input: (a) configuration #1 (I1) – the input aperture is formed by the consequent shift of one and three rows of pins with $1.5P_{EBG}$ shift of the first row (the inset demonstrates a ridge structure in the transition region); (b) configuration #2 (I2) – the input aperture is formed by the consequent shift of two and two rows of pins with $1.5P_{EBG}$ shift of the first row; (c) configuration #3 (I3) – the same as configuration #2 but with $2.5P_{EBG}$ shift of the first row. The instantaneous E-field distributions are given at 95 GHz.

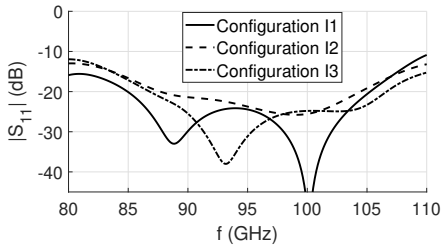

Fig. 7. Input reflection coefficient for the three configurations from Fig. 6. Design parameters (in μm): $L_{m0}^{in(1,2,3)} = 324, 573, 653$, $L_{m1}^{in(1,2,3)} = 1063, 987, 1036$, $L_{m2}^{in(1,2,3)} = 966, 855, 903$, $H_{m1}^{in(1,2,3)} = 621, 629, 619$, $H_{m2}^{in(1,2,3)} = 410, 371, 382$.

B. Amplitude and Phase Distributions Analysis

Fig. 10 presents the output amplitude and phase distributions for different QO feed configurations. In this plot, we also demonstrate analytical curves approximating elements amplitude (A_i) and phase (φ_i) according to the cosine-on-pedestal and cylindrical phase front models [5]:

$$A_i = C + (1 - C)\cos\big(\pi x_i/(N_x d_x)\big). \quad (2)$$

$$\varphi_i = -2\pi/\lambda\big(\sqrt{x_i^2 + F^2} - F\big),\ i = 1...N_x. \quad (3)$$

where C is the parameter defining the amplitude taper. As seen, the configuration with I2 input realizes almost ideal cylindrical phase distribution with 16 dB amplitude taper. When I1 input is employed, the taper can be reduced. However, the amplitude distribution becomes more frequency-dependent. This is due to a complex modal content of the radial GGW. For the elongated output configuration O2, the taper can be further reduced to 10–12 dB.

IV. Conclusion

In this contribution, we have considered the quasi-optical (QO) feeds for mm-wave linear (sub-)array antennas in gap waveguide (GWG) technology. The holistic design approach has been introduced that relies on the design decomposition principle where both input and output transition parts can be developed using the dedicated electromagnetic models with reduced simulation complexity. The approach has been utilized to develop and investigate several W-band GWG QO feeds with different input and output configurations. The obtained simulation results evidence wideband (85–105 GHz) and low insertion-loss (< 0.5 dB) feed performance with stable transmission characteristics (± 1 dB maximum frequency ripple). Future research directions will address additional methods for amplitude and phase distributions control.

Acknowledgment

This work has received funding from the European Union's Horizon 2020 research and innovation programme under the Marie Skłodowska-Curie grant agreement No 860023 and the Sweden-Taiwan Collaborative Research Framework Project "Antenna Technologies for Beyond-5G Wireless Communication" from the Swedish Foundation for Strategic Research.

References

[1] "European vision for the 6G network ecosystem," White Paper, The 5G Infrastructure Association, Jun. 2021.

[2] M. Ivashina, A. Vilenskiy, H.-T. Chou, J. Oberhammer, and M. N. M. Kehn, "Antenna technologies for beyond-5G wireless communication: Challenges and opportunities," in *Proc. 2021 International Symposium on Antennas and Propagation*, Taipei, Taiwan, Oct. 2021, pp. 1–2.

[3] T. S. Rappaport, Y. Xing, O. Kanhere, S. Ju, A. Madanayake, S. Mandal, A. Alkhateeb, and G. C. Trichopoulos, "Wireless communications and applications above 100 GHz: Opportunities and challenges for 6G and beyond," *IEEE Access*, no. 7, pp. 78 729–78 757, 2019.

[4] S. Shahramian, M. J. Holyoak, A. Singh, and Y. Baeyens, "A fully integrated 384-element, 16-tile, W-band phased array with self-alignment and self-test," *IEEE Journal of solid-state circuits*, vol. 54, no. 9, pp. 2419–2434, 2019.

[5] A. R. Vilenskiy, E. Galesloot, Y. Zhang, A. Bart Smolders, and M. V. Ivashina, "Quasi-optical beamforming network for millimeter-wave electronically scanned array antennas with 1-bit phase resolution," in *Proc. 2021 15th European Conference on Antennas and Propagation (EuCAP)*, 2021, pp. 1–5.

[6] A. R. Vilenskiy, M. N. Makurin, and C. Lee, "Phase distribution optimization for 1-bit transmitarrays with near-field coupling feeding technique," in *Proc. 14th European Conference on Antennas and Propagation, (EuCAP 2020)*, Copenhagen, Denmark, Mar. 2020, pp. 1–5.

[7] A. U. Zaman and P.-S. Kidal, *Gap Waveguide in Handbook of Antenna Technologies*. New York, NY: Springer Science+ Business Media Singapore, 2015, p. 464.

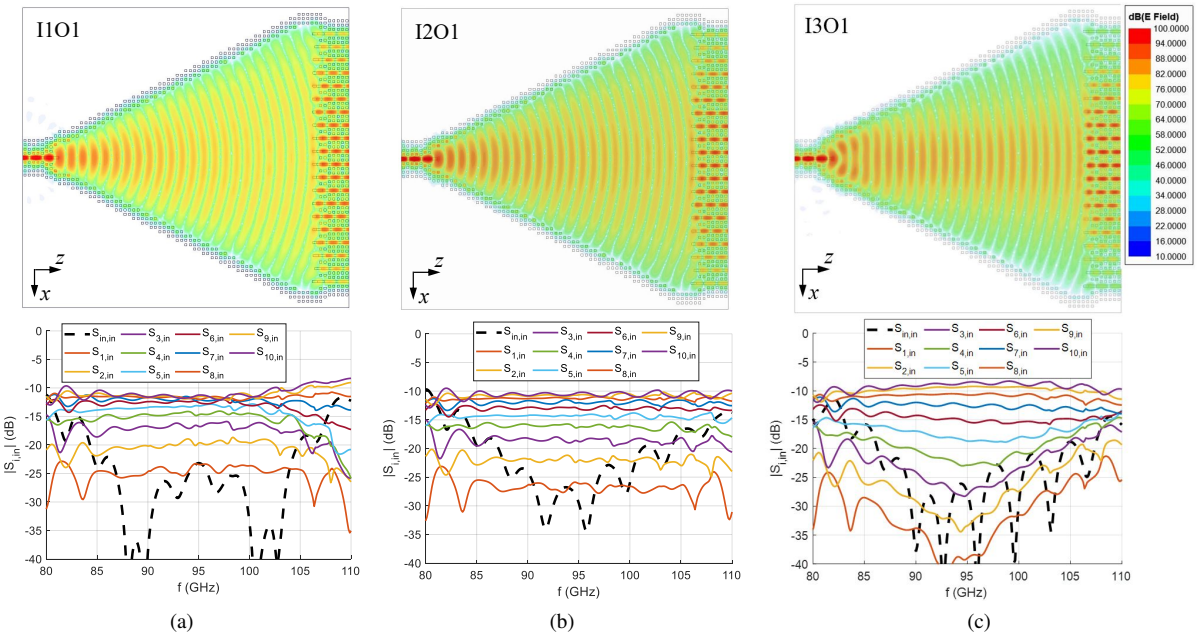

Fig. 8. Different configurations of the full QO feed and corresponding S-parameter magnitudes: (a) configuration I1O1; (b) configuration I2O1; (c) configuration I3O1. The instantaneous E-field distributions are given at 95 GHz (input port excited).

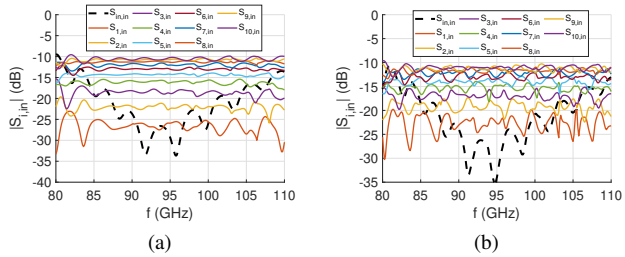

Fig. 9. Frequency performance of (a) configuration I2O1 without optimized edge elements, (b) configuration I2O3.

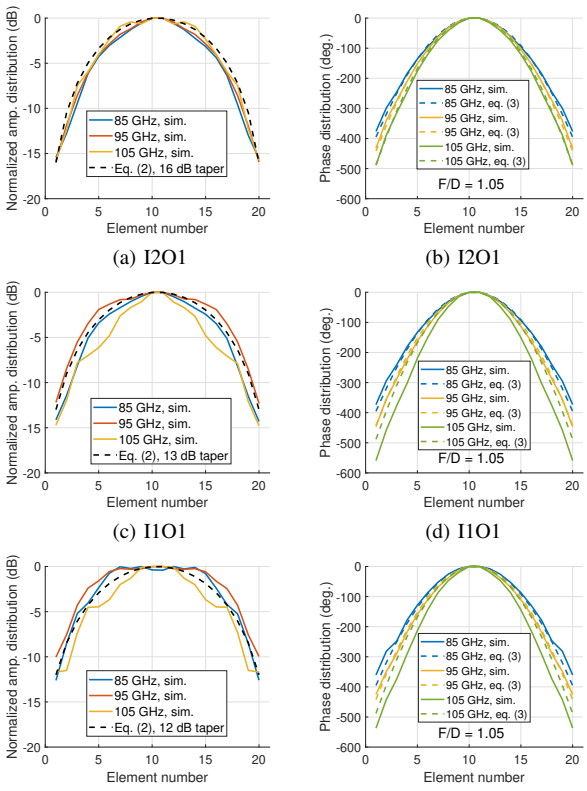

Fig. 10. Amplitude (left) and phase (right) distributions for different QO feed configurations.

[8] Y. Zhang, A. R. Vilenskiy, and M. V. Ivashina, "W-band waveguide antenna elements for wideband and wide-scan array antenna applications for beyond 5G," in *Proc. 2021 15th European Conference on Antennas and Propagation (EuCAP)*, 2021, pp. 1–5.

[9] E. Sabbaghi, S. A. Razavi, and M. H. Ostovarzadeh, "Wide band ridge gap waveguide (RGW) fan beam antenna with low side lobes based on parabolic reflector principle," *IET Microwaves, Antennas & Propagation*, vol. 14, pp. 343–347, 2020.

[10] W. Yuan, J. F. Chen, C. Zhang, W. X. Tang, L. Wang, Q. Cheng, and T. J. Cui, "Glide-symmetric lens antenna in gap waveguide technology," *IEEE Transactions on Antennas and Propagation*, vol. 68, no. 4, pp. 2612–2620, Apr. 2020.

[11] A. R. Vilenskiy, Y. Zhang, and M. V. Ivashina, "Methods for attenuating and terminating waves in ridge gap waveguide at W-band: Carbon-loaded foam, carbonyl iron paint, and nickel plating," in *Proc. 51 European Microwave Conference (EuMC)*, 2021, pp. 1–5, in press.

[12] A. K. Bhattacharyya, *Phased array antennas: Floquet analysis, synthesis, BFNs and active array systems*. John Wiley & Sons, 2006.